International Journal of Greenhouse Gas Control 137 (2024) 104195

Contents lists available at ScienceDirect

International Journal of Greenhouse Gas Control

journal homepage: www.elsevier.com/locate/ijggc

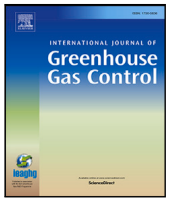

X-ray translucent reaction cell for simulation of carbon mineral storage reservoir environments

Ian D. Watt [a,*], Ian B. Butler [a], James Gilgannon [a,d], Lucas Martins [b], Florian Fusseis [c], R. Stuart Haszeldine [a], Ian Molnar [a], Stuart M.V. Gilfillan [a]

[a] School of Geoscience, University of Edinburgh, United Kingdom
[b] School of Informatics, University of Edinburgh, United Kingdom
[c] Division of Earth Sciences and Geography, RWTH Aachen, Germany
[d] School of Geographical and Earth Sciences, University of Glasgow, United Kingdom

ARTICLE INFO

Keywords:
CO_2 mineralization
Geological CO_2 storage
4DμCT
Reservoir simulation

ABSTRACT

Understanding how in-situ mineralization of CO_2 affects the porosity, permeability, and pore network of the host rock is critical to assessing the viability of basalt reservoirs as carbon dioxide repositories. Here, we present an x-ray translucent environmental cell which allows carbon mineralization, and other fluid–rock reactions to be studied in real time and on the grain scale under simulated geological reservoir conditions using microtomographic imaging. The cell operates autonomously from a CT instrument and is periodically quenched and relocated for scanning, enabling long duration operando experiments. Samples are reacted under controlled conditions of chemistry, temperature, and fluid pressure. Porosity and permeability changes are tracked through digital image analysis of successive CT scans. Samples are fully recoverable, allowing for a suite of post-mortem analyses. The cell design uses readily available materials, can sustain long-term operating temperatures of up to 200 °C, and is reproducible at low cost with a centre lathe and a mill using a conveniently equipped mechanical workshop.

1. Introduction

The Intergovernmental Panel on Climate Change (Benson et al., 2018; Shukla et al., 2022) and other prominent scientific institutions (IEA, 2022; Committee on Climate Change, 2019) have stated that large-scale carbon capture and storage is essential to mitigate the worst effects of anthropogenic climate change and meet nationally declared net-zero targets (UNFCCC). Currently, 44 Mt of CO_2 are captured and stored annually in geological formations by engineered operations (IEA, 2022). This rate must increase approximately 100-fold by mid-century to meet internationally agreed climate commitments. The Carbfix project in Iceland (Snæbjörnsdóttir et al., 2020), where aqueous CO_2 is injected into basalt to engineer the precipitation of solid carbonate minerals as a permanent means of CO_2 storage, is the world's foremost CO_2 mineralization operation, aiming to store 3 Mt CO_2 per year by 2031. The successful development of Carbfix, which was only proposed as an operational idea in 2006, has driven interest in a wider application of CO_2 storage by mineralization (Nelson et al., 2022; Kumar et al., 2017; Raza et al., 2022).

The mineralization of injected CO_2 is confirmed at Carbfix by analysis of post-injection formation fluids, combined with chemical and isotopic tracer testing, and computer modelling (Clark et al., 2020; Ratouis et al., 2022). The depth and extent of the geothermal field which serves as the carbon mineral reservoir at Carbfix renders physical sampling and direct observation of the reaction impracticable (Gunnarsson et al., 2018). This predicament will hold true for any large-scale prospective carbon mineral storage (CMS) site. Therefore, realistic bench-top physical simulations of reservoir environments must be developed to build a comprehensive understanding of how the mineralization reaction proceeds *in-situ*.

To date there have been a number of laboratory studies investigating the CO_2-water-rock reaction that underpins the carbon mineralization process, but these typically focus on promoting the reaction on a short timescale or compromise on simulated reservoir conditions. This could include using powdered or sintered material in place of whole rocks to maximize surface area or generate a pre-existing fracture network, respectively (Galeczka et al., 2014; Gadikota et al., 2020; Voigt et al., 2021; Hellevang et al., 2017). Quenched whole rock cores have also been employed in batch reactions, with X-ray microtomographic imaging utilized only at the beginning and end of experiments (Kanakiya et al., 2017; Xiong et al., 2018, 2017).

* Corresponding author.
E-mail address: ian.watt@ed.ac.uk (I.D. Watt).

https://doi.org/10.1016/j.ijggc.2024.104195
Received 19 April 2024; Received in revised form 28 June 2024; Accepted 1 July 2024
Available online 31 July 2024

Monomineralic reactants such as olivine or wollastonite (Menefee and Ellis, 2021; Zhu et al., 2016; Wang et al., 2019; Xiong et al., 2018), are commonly used in place of a polymineralic basalt which is assumed to show slower reaction kinetics (Snæbjörnsdóttir et al., 2020; Gislason and Oelkers, 2003). Those studies which have used whole pieces of basalt and a flowing reactive fluid have not included time series images of the reaction process, using μCT only before and after the respective experiments (Menefee et al., 2019; Luhmann et al., 2017a,b; Adeoye et al., 2017). The few time-resolved X-ray computed tomography (4DμCT) experiments investigating mineral carbonation and associated evolution of rock properties have been time-limited to several days (Zhu et al., 2016; Xing et al., 2018), due to the limited duration of beamtimes available at synchrotron facilities. Accordingly, some combination of the steps listed above have been taken to ensure the mineralization reaction occurs within the required time-frame. The aim of the presented experimental cell and method is to create a simulated geological reservoir environment with elevated conditions of pressure and temperature. The design is intended for use with laboratory microtomography instruments which provides for 4D visualization of reaction progress without the need to compromise chemical conditions or material properties to increase reaction rates.

Important questions remain about how the mineralization reaction proceeds under ranges of temperature, fluid composition, pH, pCO_2, and reservoir rock composition. These include an understanding of which carbonate mineral phases predominate under different conditions, the additional types of secondary minerals precipitated and how these may affect further carbonate precipitation (Sissmann et al., 2014), reaction kinetics (Gysi, 2017), the evolution of reservoir porosity and permeability (Callow et al., 2018), and the potential of non-mafic igneous rocks for carbon mineralization (Marieni et al., 2018).

To address these questions, we have developed an X-ray translucent flow cell designed to simulate an engineered carbon mineral storage (CMS) reservoir by introducing fluids to a sample of rock under elevated pressure and temperature conditions. The cell enables near a real-time investigation of the carbonate mineralization reaction, and has been tested at temperatures up to 200 °C. Whole rock cores are held within an X-ray translucent casing and reaction progress is tracked by 4DμCT after fluids have percolated through the rock core at set intervals. The cell is designed to operate with apparatus independent of a microtomography instrument, and to only be relocated for the duration of a scan. Thus, long term experiments providing 4D imaging datasets are practicable. Here, we present example data from an experiment which ran for 13 weeks, and are confident in the feasibility of significantly longer duration. The cell is made of inexpensive and readily available materials, and is simple to reproduce as all components can be manufactured in a mechanical workshop equipped with a centre lathe and a mill. The principal objective of the cell is to investigate the cumulative effect of fluid–rock reaction and mineral precipitation on basalt porosity and permeability, as well as provide insight into the role of non-carbonate precipitates in a CMS subsurface environment. Data and insights generated from bench-top reservoir simulations using the presented apparatus will improve understanding of CMS reservoir environments and inform decisions regarding the potential deployment of this technology beyond Iceland.

2. Materials and methods

2.1. Cell design and materials

The experimental cell has been designed to be easily reproducible. The main cell body is comprised of a single piece of 6061-T6 aluminium alloy bar, with the end caps and supporting base made of corrosion resistant 316 stainless steel. Aluminium was chosen for its low X-ray attenuation, efficient thermal conductivity, and wide availability. The tensile strength of 6061 aluminium shows significant variability with heat exposure time between 125 and 300 °C (Czerwinski, 2020; Farrell, 1995), but can operate at temperatures and pressures higher than semicrystalline thermoplastic (Kahl et al., 2016). The presented cell could operate for >100,000 h at up to 200 °C and 50 bar pressure, with a large margin of safety. Temperatures >200 °C and pressures >100 bar are also safely attainable but are dependent upon exposure time. See Supplementary Material for further details on time components of material strength.

An inert and X-ray translucent polytetrafluoroethylene (PTFE) sleeve occupies the central borehole of the aluminium cell and is used to ensure reactant fluids remain out of contact with the aluminium pressure vessel. The PTFE sleeve is split into two chambers, the upper chamber is designed to house granular material or cylindrical cores of rock of diameter 10 mm and maximum height 20 mm. Mulitple cores can also be stacked inside the imaging chamber to a maximum height of 20 mm. Alternatively, a chemically inert and suitably heat resistant material such as PTFE can be used to pack the imaging chamber space and accommodate 10 mm discs of any thickness an eliminate empty space. Equally, a core of diameter <10 mm could be accommodated with a bespoke sleeve of PTFE or other suitable material to pack out the internal volume of the imaging chamber. The aluminium cell walls are reduced to 2 mm thickness at the imaging section surrounding the rock core to reduce X-ray attenuation (S, Fig. 1). A removable two-part aluminium collar fits the concave external section to leave a uniform cylindrical surface to be heated by means of band heaters during the experiment (Fig. 1 and Supplementary Material Pages 1 and 9).

The larger, lower chamber of the PTFE sleeve (R, Fig. 1) allows for an initial reaction of injection fluid with a solid phase reactant to modify the properties of the injection fluid at the operating temperature. In the presented methodology, basalt particulate is used to promote a reaction with the fluid which provides the necessary cations for carbonate formation and buffers pH (Snæbjörnsdóttir et al., 2020). Crushed rock is used to maximize reactive surface area, however, any suitable pre-reactant material could be utilized in the presented design. The two chamber cell design is an attempt to simulate the subsurface environment at CMS operations on a bench-top scale. In the field, a dissolution dominant environment persists at the injection zone, serving to both liberate critical cations from the reservoir rock and maintain injectivity. Carbonates are precipitated after an ion exchange was facilitated between fluid and rock along the flow path and fluid pH is buffered through mixing with formation fluids (Ratouis et al., 2022; Clark et al., 2020). Placing the two chambers adjacent within the same heated pressure vessel eliminates the risk of precipitation due to fluid temperature variation between chambers.

Stainless steel socket screws attach the steel end caps to the main cell body. The cell is sealed with evolast N894 FFKM perfluoroelastomer (MCM High-Performance Sealing) o-rings and PTFE plugs (Fig. 1 and Supplementary Material Pages 1, 3, 4, and 5). The evolast N894 o-rings have a typical operating range of −25 to +270 °C. It was evidenced that although the widely available “viton” perfluoroelastomer o-rings provided an effective initial seal at temperatures up to 170 °C, the seals repeatedly failed under subsequent cyclic heating and cooling. The bore seal configuration is critical to enable the cyclic heating and cooling of the cell required for facilitation of CT scans (Supplementary Material). Fluids are introduced to the cell via 1/16" polyetheretherketone (PEEK) tubes and high pressure liquid chromatography fittings (HPLC) machined directly into the steel end caps. Needle valves (Swagelok) allow the cell to be sealed and detached from the rest of the apparatus for CT scanning.

Fluid flow and pressurization are enabled by an LC-5000 500 ml capacity syringe pump (Teledyne ISCO), flowing against a 0–500 psi variable backpressure regulator (Swagelok). The pump delivers fluid through the base of the cell into the large mixing chamber. Fluids then pass through a bore in the PTFE sleeve and a 20 μm PTFE column frit (Cole Parmer) into the rock core occupying the imaging chamber. The column frit prevents the exchange of solid material between the upper and lower chambers. Outflow fluids are passed through an external 2

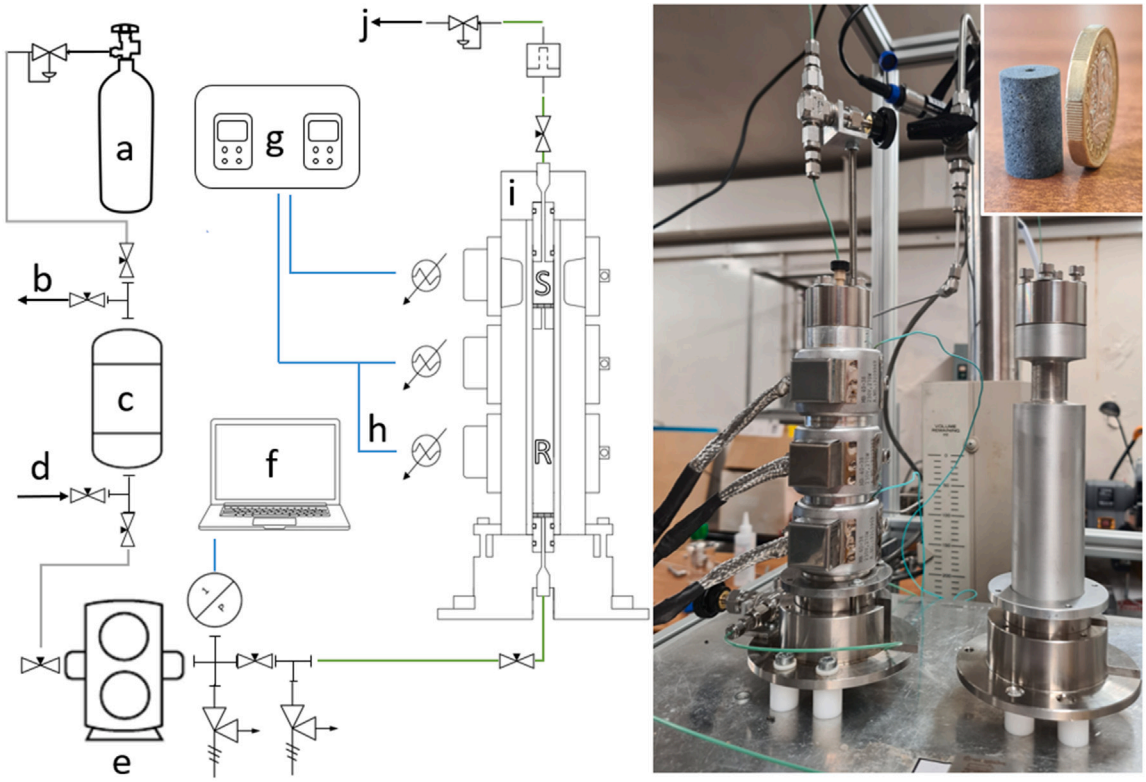

Fig. 1. Right: Two cells on bench top, one under pressurized operation with attached band heaters, the second unconnected with the X-ray imaging window exposed. **Top Right, insert:** example of prepared basalt sample with coin for scale. **Left:** Process and instrumentation diagram of experimental setup. Standard symbol legend provided in Supplementary Material. Silver lines indicate 1/8" Swagelok tubing, green lines 1/16" PEEK tubing and blue lines are electric cabling. **a**: CO_2 canister. **b**: Purge valve. **c**: Mixing pressure vessel. **d**: Loading valve for fluids. **e** Teledyne ISCO geared pump. **f** Pressure monitoring and logging. **g** Watlow PID heater control unit. **h** Band heaters. **i** Experimental cell main body. **j** Outflow fluid collection. **R**: Pre-reaction chamber. **S**: Sample chamber for imaging.

μm filter (Swagelok) and the variable backpressure regulator before collection for sampling or disposal. A 250 psi pressure relief valve at the pump outlet is used to relieve fluid pressure if there is a rise in pressure caused by a blockage. A sprung pressure relief valve set to 1000 psi (Swagelok) fixed within the pump chamber system serves to protect the pump from overpressure in the event that tubing or the 250 psi relief valve become blocked. A purge valve above the mixing pressure vessel allows pressurized CO_2 to be purged from the system through a neutralizing tank of 0.25 M NaOH solution. Gaseous CO_2 concentration in the laboratory air is constantly monitored with a high sensitivity sensor (Analox) linked to an audiovisual alarm system set to trigger from 1000 ppm. Constant pressure monitoring of the closed experimental system is logged by a digital pressure transducer (ESI Technology) connected to a Windows PC. See Fig. 1 for diagrammatic representation of all components.

Heating is provided to the cell by three 270 W band heaters (RS PRO) regulated by two proportional integral derivative controllers (PID, Watlow) using type K thermocouples (Omega). The band heaters allow for a compact design that enables multiple cells to occupy bench-top space and operate at independent temperatures. Band heaters and aluminium collar pieces are removed prior to CT scanning.

A sample of Faroese picrite of approximately 56 million years in age (Larsen et al., 1999) was used for a demonstrative test of the cell's function. The picrite was chosen due to its high potential reactivity as a result of its mainly unaltered state and high content of primary olivine and pyroxene. As the sample displayed < 1% porosity, a borehole of 1.5–2 mm diameter was drilled in the 10 mm diameter core to ensure a fluid connection between the pumped fluid and backpressure regulator. The rock core was designed as a tight fit into the PTFE sleeve within the aluminium cell, which is machined with a 9.9 mm diameter. This prevents any unwanted core movement during rotation while CT scanning and relocation between the laboratory bench and the optical table. A two-phase experiment was conducted at 170 °C where de-ionized water equilibrated with 10 bar CO_2 was injected for 1068 h, followed by an aqueous solution of 0.64 M $NaHCO_3$ equilibrated with 10 bar pCO_2 for 1167 h. A 10 bar CO_2 pressure was chosen to approximate the injection fluid conditions at Carbfix2, where a 9 bar PCO_2 is used (Gunnarsson et al., 2018).

The sample material used within the cell is not limited to whole rock cores. The cell will also function equally well using granular material. This could be of particular interest for simulation experiments relating to ex-situ mineral carbonation processes, or subsurface environments where target formations are particularly fine-grained, such as hyaloclastite layers in basalt flows. The use of 10 mm diameter hydrophilic PTFE column frit filters at the base of the S chamber (Fig. 1), prevents the transport of material >20 μm between vessel chambers.

3. Data acquisition

3.1. Computed tomography configuration

Tomographic data were acquired on a custom manufactured cone beam microtomography instrument using a peak energy of 120 kV and 24 W target power loading. 2000 projections were acquired with a 2 s exposure through a single 360° turn of the rotary table. Raw data were collected using a Perkin-Elmer XRD0822 flat panel 1 megapixel amorphous silicon X-ray detector with a terbium-doped gadolinium oxysulfide scintillator. After each scan was complete the cell was returned to the bench-top flow apparatus for the experiment to continue. Raw μCT data were reconstructed using Octopus Reconstruction v8.9 (Vlassenbroeck et al., 2006) software to produce 906 16-bit Tag Image File Format images with a voxel size of 9.84 μm. This equates to a digital representation of a 9.5 mm cylindrical section from the centre

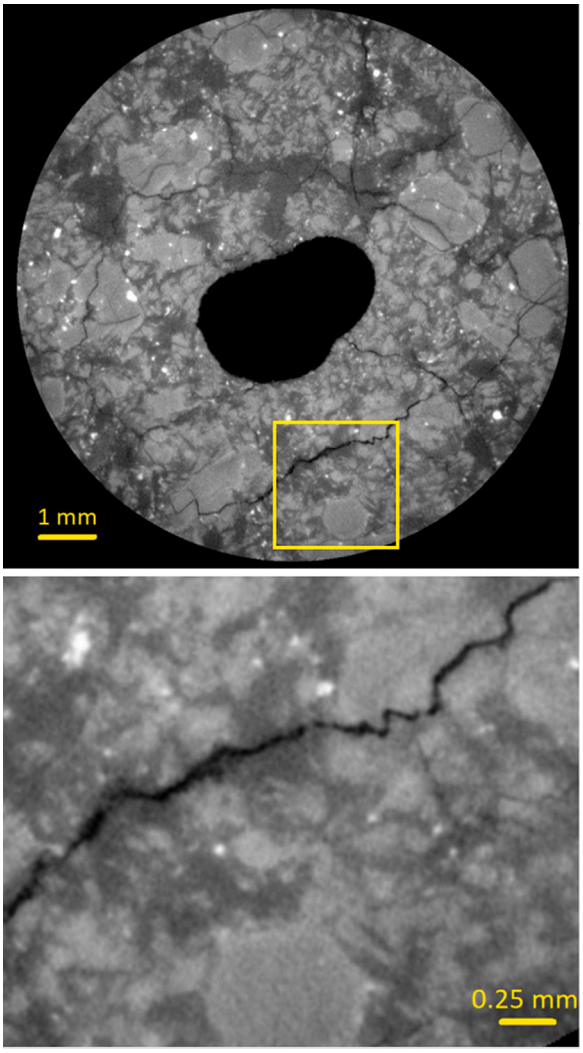

Fig. 2. Above: Showing features resolvable in reconstructed images. Mineral phases, nascent fractures, and interface between central bore and rock matrix are sharply defined. **Below**: Higher magnification image of fine features. No image filtering has been applied to the reconstructed data.

of the picrite core. Digital image analysis of reconstructed images was performed in ORS Dragonfly build 2022.1 under a free-to-use academic license.

3.2. Core recovery and scanning electron microscopy

The PTFE sleeve lining the cell allows for the recovery of intact rock cores and subsequent post-mortem analyses. As the dissolution and precipitation reactions associated with mineral carbonation can cause fracturing within the host rock (Zhu et al., 2016), care must be taken when recovering the core. The PTFE sleeve was cut above the core and below the join between the upper and lower chambers, facilitating access to top face of the core. EpoThin 2 epoxy resin (Buehler) was then injected under vacuum to permeate the central bore and connected porosity. Once the resin had set the PTFE sleeve was readily cut away, leaving a structurally sound whole core which could be subjected to post-mortem analyses. Here, we elected to cut the core into slices and set these in resin blocks as polished sections to enable SEM analyses of the interior of the sample and ground-truthing

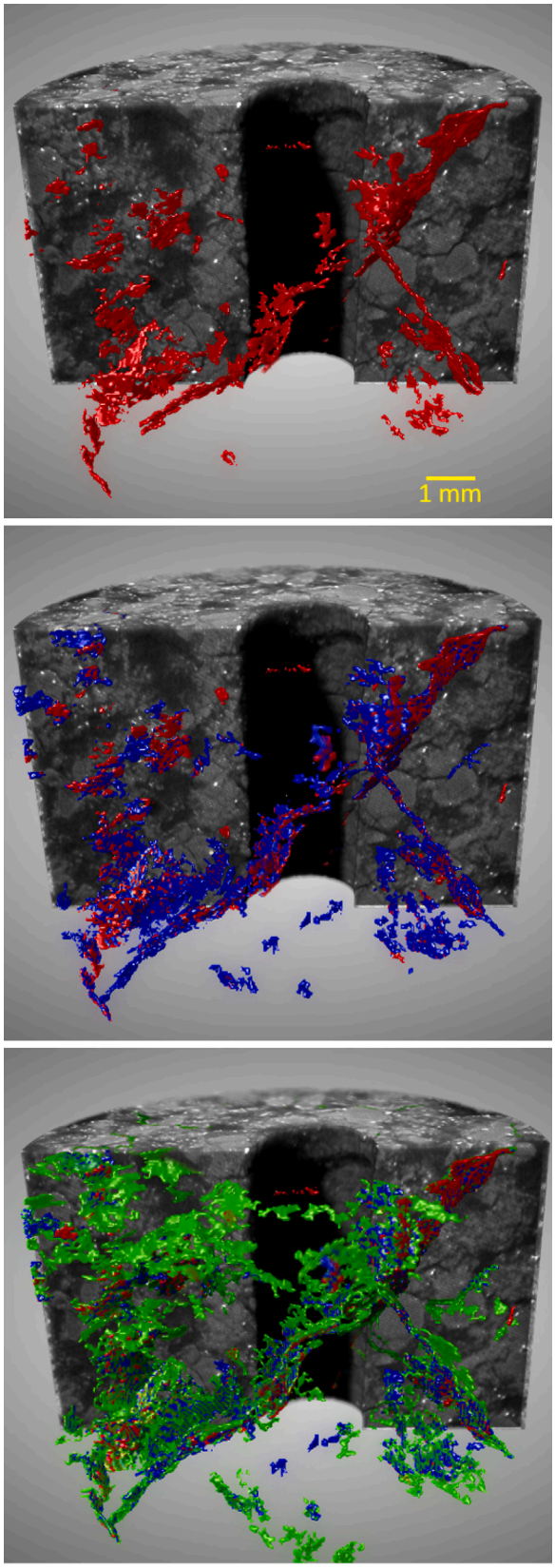

Fig. 3. 3D rendering of picrite core a different time steps during the experiment, with visual clipping (ORS Dragonfly). **Above**: A segmentation of the fracture network at 0 h (red) of the $NaHCO_3$ injection phase. **Middle**: Fracture extent after 200 h (blue), imposed on 0 h fracture segmentation. **Below**: Fracture extent after 1167 h (green), imposed on 200 h and zero hours fracture segmemtations.

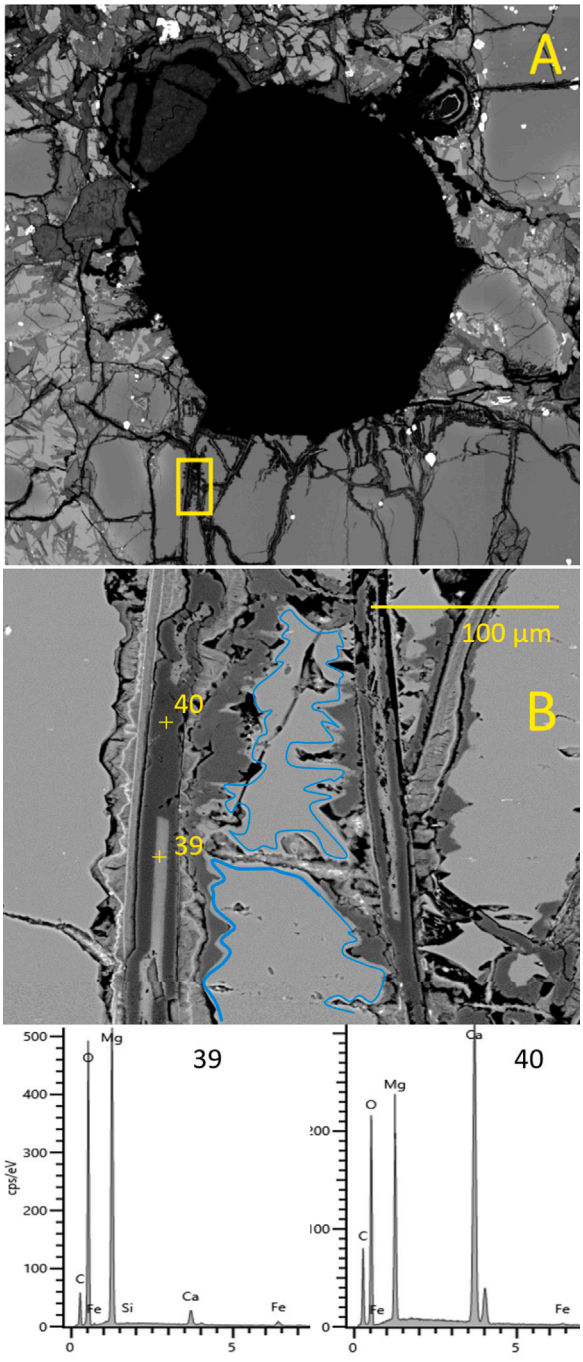

Fig. 4. A. Cropped backscatter electron image of post-experiment picrite. Fractures are newly formed during experiment and predominantly infilled with newly formed carbonates. B showing carbonates and associated spectra. Reaction front evident in central olivine grain.

of CT datasets. Carbonate minerals have X-ray attenuation properties very similar to plagioclase feldspar and clinopyroxene, primary basaltic minerals (Hanna and Ketcham, 2017). SEM analyses can identify the composition of carbonates formed and assist in the segmentation of CT images by visual comparisons or calculation of attention values for observed carbonate chemistry. SEM analyses were conducted with a Carl Zeiss Sigma HD VP field emission SEM using an accelerating voltage of 15 kV and a 7 mm working distance.

3.3. Example data

An unfiltered transverse µCT slice of the picrite core during the flow experiment is shown in Fig. 2, to demonstrate the ability of the cell to resolve fine features of the imaged material. Significant improvements can be attained through image filtering to isolate particular features. For example, local contrast enhancement algorithms within ORS Dragonfly, e.g. CLAHE, are particularly effective at accentuating microfractures within the sample. Fig. 3 shows a 3D rendering of the picrite core at different time steps of the experiment, achieved using ORS Dragonfly. The cores have been visually clipped to expose segmentations of the expanding crack network.

A cropped back-scatter electron image of a transverse slice of the post-experiment picrite core is shown in Fig. 4 to demonstrate the additional capabilities for post-mortem analyses of the presented methodology. EDX spectra of secondary mineral phases infilling the cracks confirm two distinct carbonate-like spectra, magnesium rich and mixed calcium–magnesium with minor iron (spectra 39 and 40, Fig. 4).

4. Conclusion

The design for an bench-top environmental cell used to simulate geological environments under dynamic fluid flow conditions is presented. The cell is capable of long term operando CT imaging experiments, without permanent fixation to a CT instrument. Example data demonstrate the utility of the cell design to investigate changing rock properties during the carbon mineralization reaction, and the potential for the same methodology to be applied to other fluid–rock reactions of interest. The design allows for 4D imaging experiments to be conducted over weeks to months, and potentially much longer, offering new insights into the evolution of geological environments over the same periods. The cell has been tested to 200 °C, and is capable of sustaining operational pressures of 100 bar at this maximum operating temperature (Supplementary Material). The cell is reproducible from the provided technical drawings using widely available materials by a conventionally equipped mechanical workshop.

CRediT authorship contribution statement

Ian D. Watt: Writing – review & editing, Writing – original draft, Visualization, Methodology, Investigation, Formal analysis, Conceptualization. **Ian B. Butler:** Writing – review & editing, Methodology, Conceptualization. **James Gilgannon:** Writing – review & editing, Software, Data curation. **Lucas Martins:** Visualization. **Florian Fusseis:** Writing – review & editing, Supervision. **R. Stuart Haszeldine:** Supervision. **Ian Molnar:** Writing – review & editing, Supervision. **Stuart M.V. Gilfillan:** Writing – review & editing, Supervision.

Declaration of competing interest

The authors declare the following financial interests/personal relationships which may be considered as potential competing interests: Ian D. Watt reports financial support was provided by Engineering and Physical Sciences Research Council. If there are other authors, they declare that they have no known competing financial interests or personal relationships that could have appeared to influence the work reported in this paper.

Data availability

Data will be made available on request.

Acknowledgements

This work was supported by an Engineering and Physical Sciences Research Council Standard Research Studentship EP/TP517884/1. The authors acknowledge the contribution of Ivan Febbrari in preparing polished thin sections of primary and post-reaction rock samples for analyses.

Appendix. Supplementary material

A.1. Strength calculations

The maximum safe operating conditions of the cell are dictated by the material properties of 6061-T6 aluminium alloy. The yield strength of this alloy degrades with length of exposure to elevated temperature (Farrell, 1995). This behaviour becomes pronounced at temperatures >150 °C. If operated at temperatures ≤150° C and a working pressure of 100 bar, total utilization of 6061-T6 yield strength (Eq. (4)) at 0.2% elongation reaches ~29% for up to 100,000 h of operation. At 200 °C and 100 bar working pressure, utilization of material yield strength at 0.2% elongation increases to 78% for up to 100,000 h of operation. For 10,000 h or less at the same conditions, utilization of yield strength at 0.2% elongation reduces to a maximum of 46%. The upper limits of required duration of these types of extended operando experiments are considered to be up to 17,500 h (two years). The controlling factor on vessel strength is the 2 mm wall thickness at the X-ray imaging window in the main cell column. As this is the location most likely to deform under load, the vessel strength is calculated using the radial dimensions at this location. Strength calculations are made modelling the cell as a closed, thick-walled cylinder and using the Lamé equations for hoop and radial stresses (Eqs. (1) & (2)) (Ayob et al., 2009).

P_i = internal pressure
P_o = external pressure
r_i = internal radius
r_o = external radius
σ_y = yield strength at 0.2%
σ_h = hoop stress
σ_r = radial stress
σ_m = total stress
M_u = material utilization

$$\sigma_h = \frac{P_i r_i^2 - P_o r_o^2}{r_o^2 - r_i^2} + \frac{(P_i - P_o) r_i^2 r_o^2}{(r_o^2 - r_i^2) r_o^2} \quad (1)$$

$$\sigma_r = \frac{P_i r_i^2 - P_o r_o^2}{r_o^2 - r_i^2} - \frac{(P_i - P_o) r_i^2 r_o^2}{(r_o^2 - r_i^2) r_o^2} \quad (2)$$

$$\sigma_m = \sigma_h - \sigma_r \quad (3)$$

$$M_u = \left(\frac{\sigma_m}{\sigma_y}\right) 100 \quad (4)$$

The minimum working pressure of the cell is dictated by the vapour pressure of water at the operating temperature of the experiment. The backpressure regulator is set to a value slightly higher to prevent the injection fluid boiling within the pressure vessel. Experimentalists wishing to copy the presented designs are advised that we conservatively suggest a maximum working pressure of 100 bar for temperatures between 150–200 °C and duration up to 10,000 h. The cell has been successfully tested in our laboratory for 496 h at 200 °C and 2235 h at 170 °C. At temperatures below 150 °C we suggest a maximum working pressure of 150 bar to limit yield strength utilization to ~33% for experimental duration up to 100,000 h of operation. We emphasize the need to consult and comply with relevant local legislation regarding the safe operation of pressurized vessels.

A.2. Technical drawings and operation

A process and instrumentation diagram with a standard symbol key is included in Fig. A.5 to supplement Fig. 1. Technical drawings for all cell components are also included below (see Fig. A.6). Top and bottom caps are machined from titanium in the presented cell, but stainless steel functions equally well as a cheaper alternative. The stainless steel baseplate presented here is designed specifically to be compatible with the mounting apparatus for the optical bench of our CT instrument. This should be considered for any CT instrument intended for cell deployment, and the baseplate designed accordingly to secure the cell. A bore seal design was adopted for the PTFE sleeve and end caps union. An earlier iteration of the cell design utilized face seals between a PTFE cap and the steel/titanium end caps, however, this design led to compression of the PTFE caps over time and a deformation of the o-ring grooves which eventually caused the seals to fail following repeated heating and cooling cycles. We recommend the replacement of all PTFE components upon completion of long duration experiments to ensure continued reliable sealing. Stainless steel high pressure liquid chromatography fittings are preferable for the inlet and outlets to the end caps. PEEK fittings can be used, but their expansion and contraction thermal response rates are different to steel/titanium to the extent that sealing failures are a possibility, particularly over the course of an extended operando experiment. The example data here were gathered using a core prepared with a borehole, however, rock samples with sufficient porosity and permeability can equally be utilized, and would indeed provide data relevant to geological reservoirs. Whilst naturally porous samples can be used, the current design does not allow for pressure gradients to be measured across the inlet and outlet of the cell.

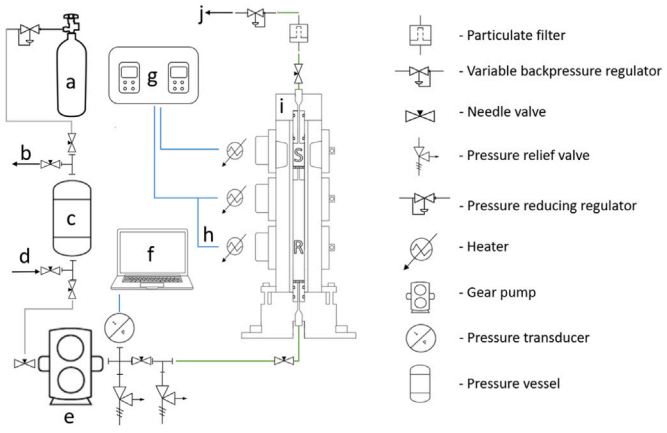

Fig. A.5. Process diagram of experimental set up with legend of Piping and Instrumentation Diagram standard symbols.

Units are in millimetres for technical drawings. M3, M4, M5 and M6 are standard metric bolt major diameters corresponding to thread radii in mm (see Fig. A.5).

Parts List			
Item	Qty	Part Number	Material
1	1	Baseplate	Stainless Steel
2	1	Bottom Cap	Titanium
3	1	Pressure vessel	Aluminum
4	1	Top Cap	Titanium
5	1	Collar	Aluminum
6	1	Clamp	Aluminum
7	1	Clamp 2	Aluminum
8	4	M5 Alloy Steel Socket Head Screw	Steel
9	4	M5 Alloy Steel Socket Head Screw (1)	Steel
10	4	M3 Alloy Steel Socket Head Screw	Steel
11	1	Sleeve	PTFE
12	1	Long Sleeve Plug	PTFE
13	1	Short Sleeve Plug	PTFE

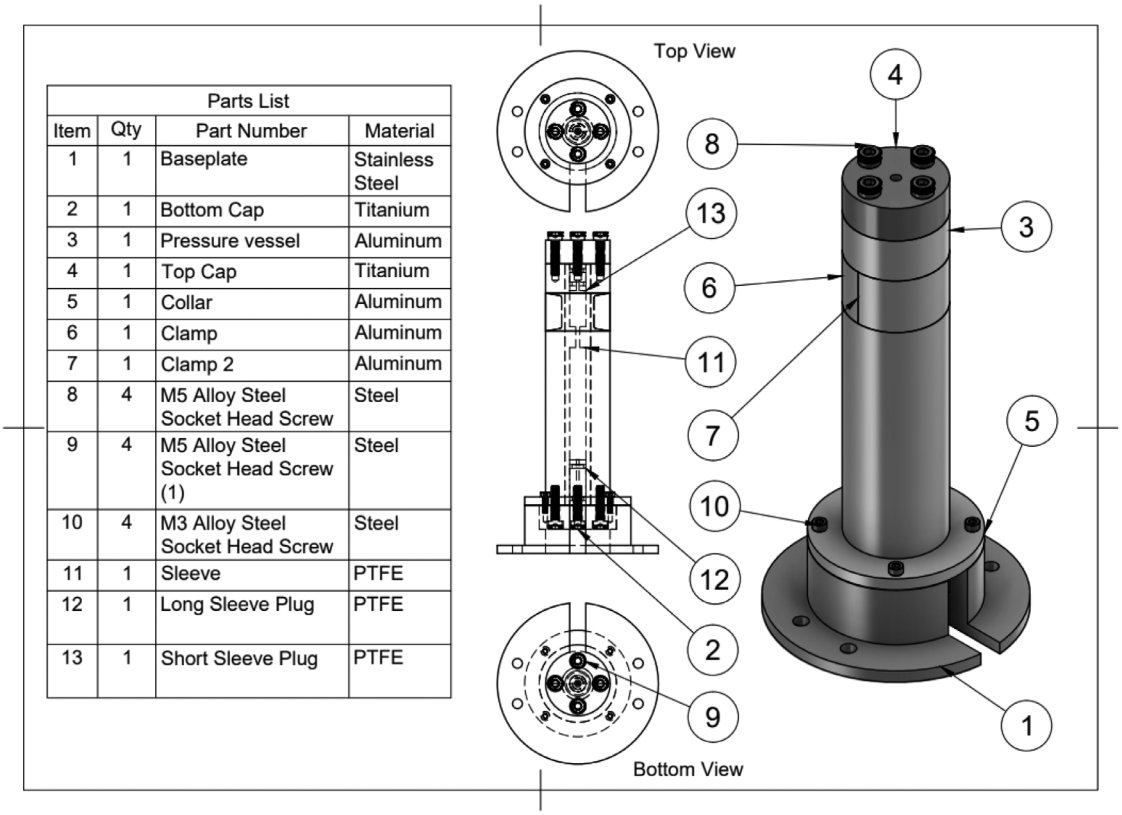

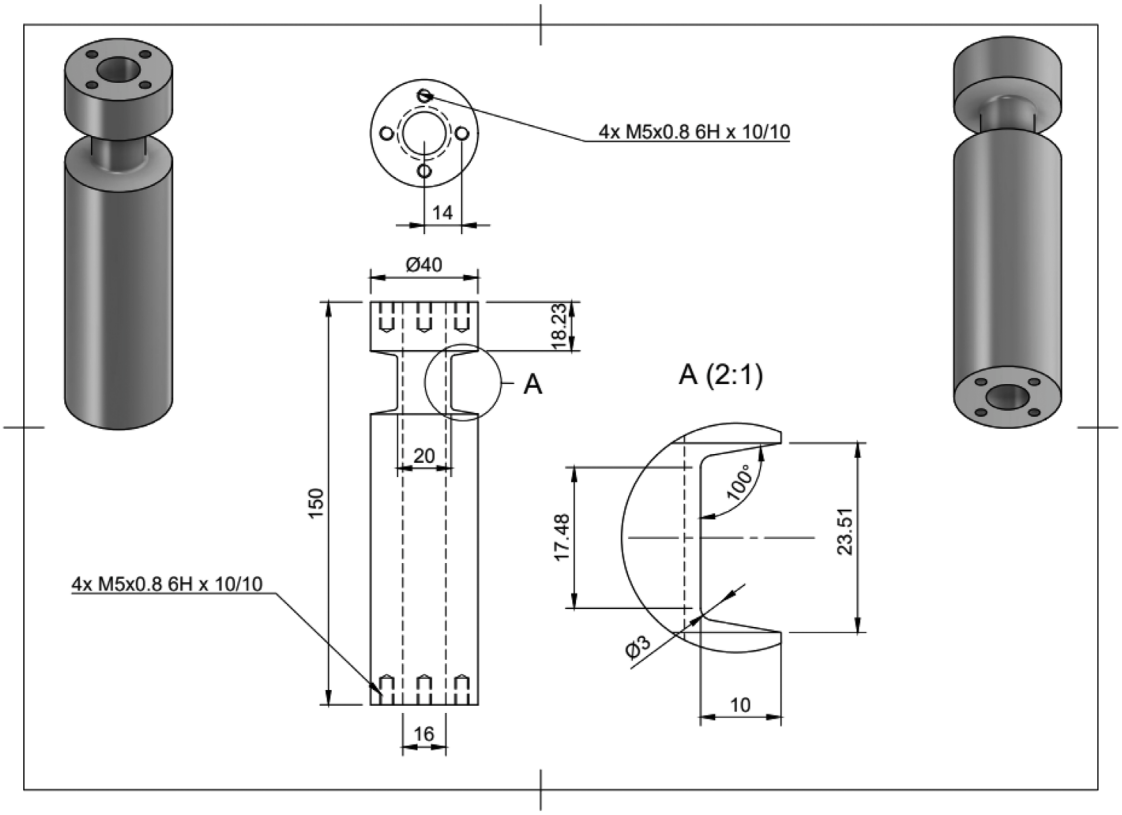

Fig. A.6. Technical drawings for cell components.

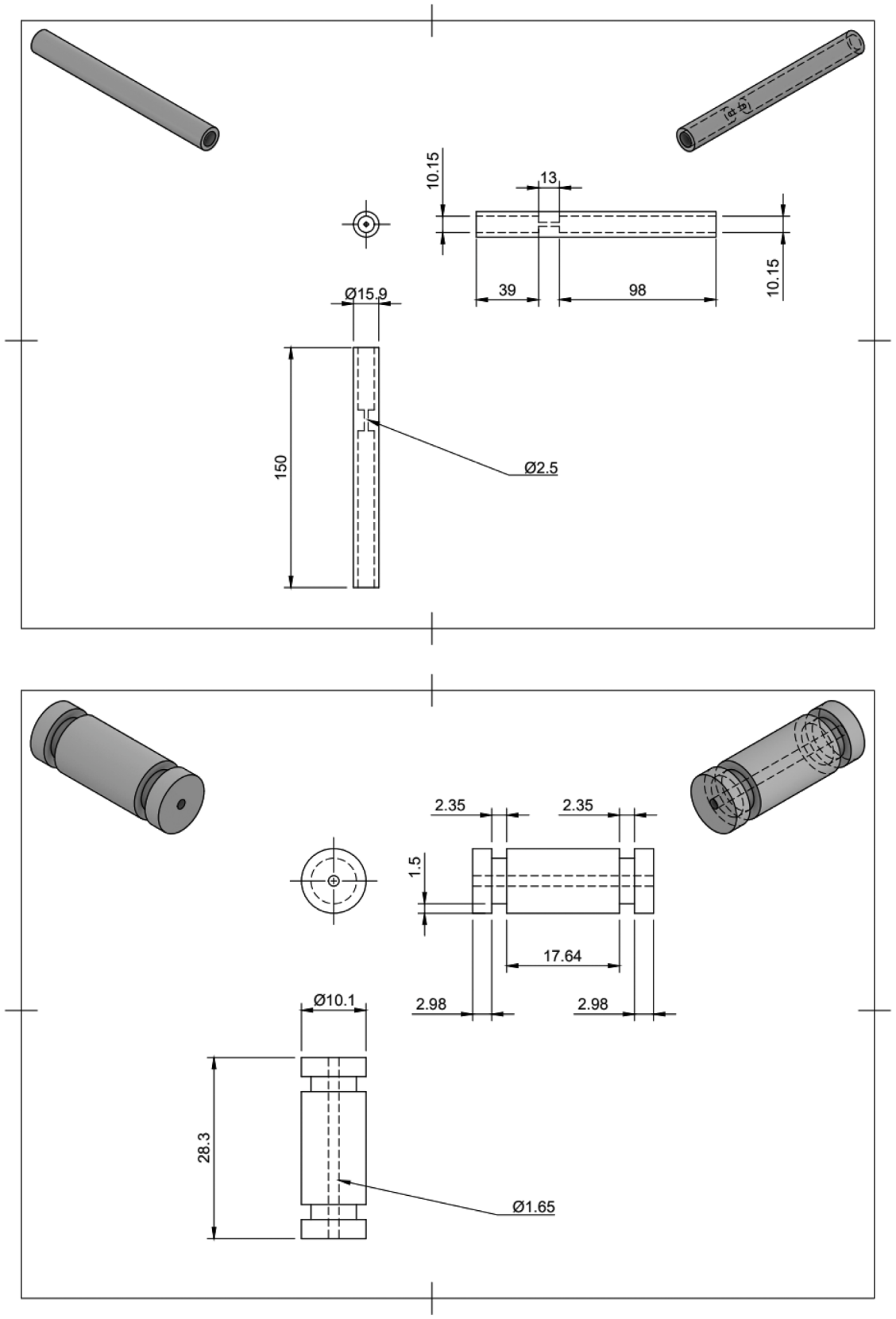

Fig. A.6. (*continued*).

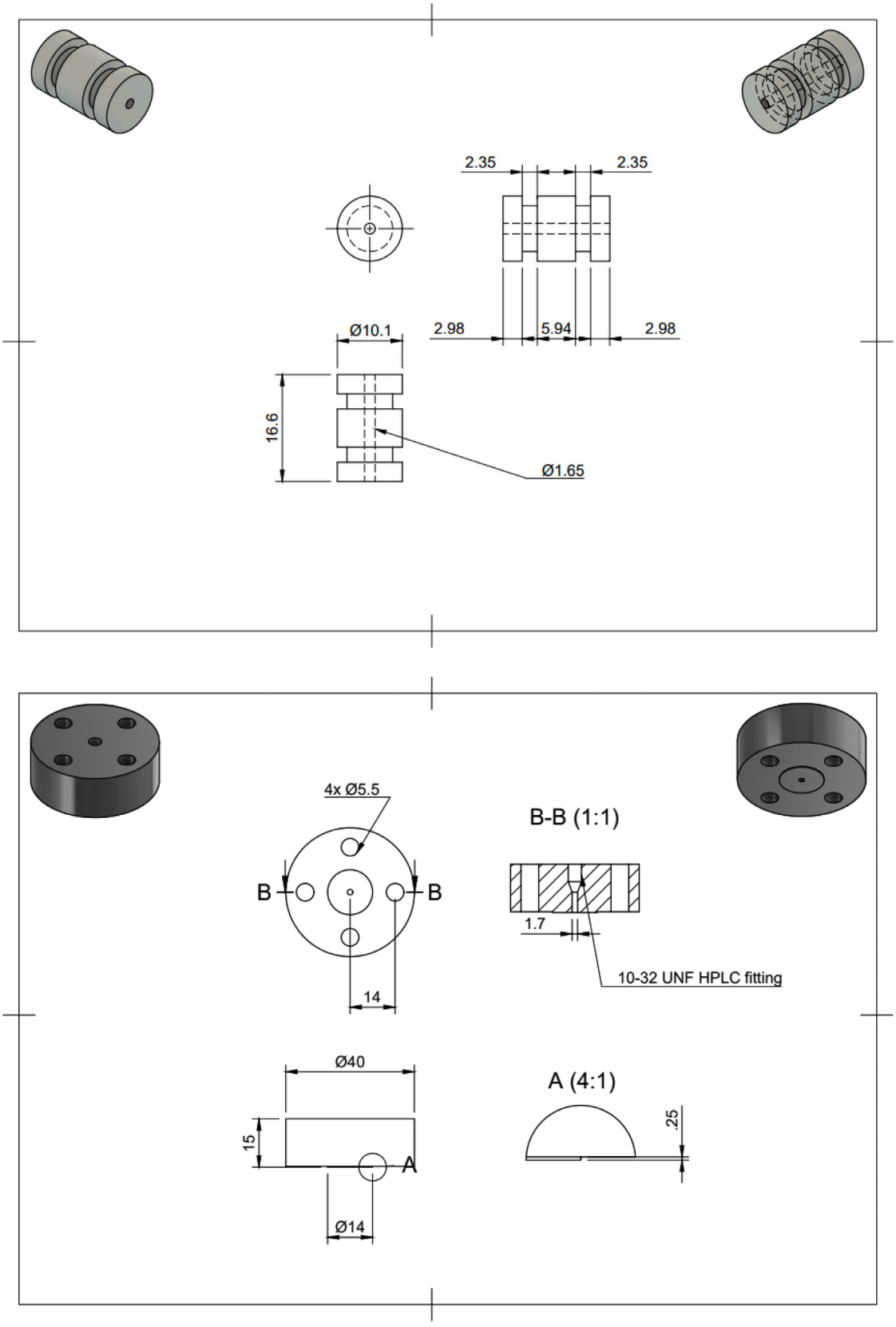

Fig. A.6. (*continued*).

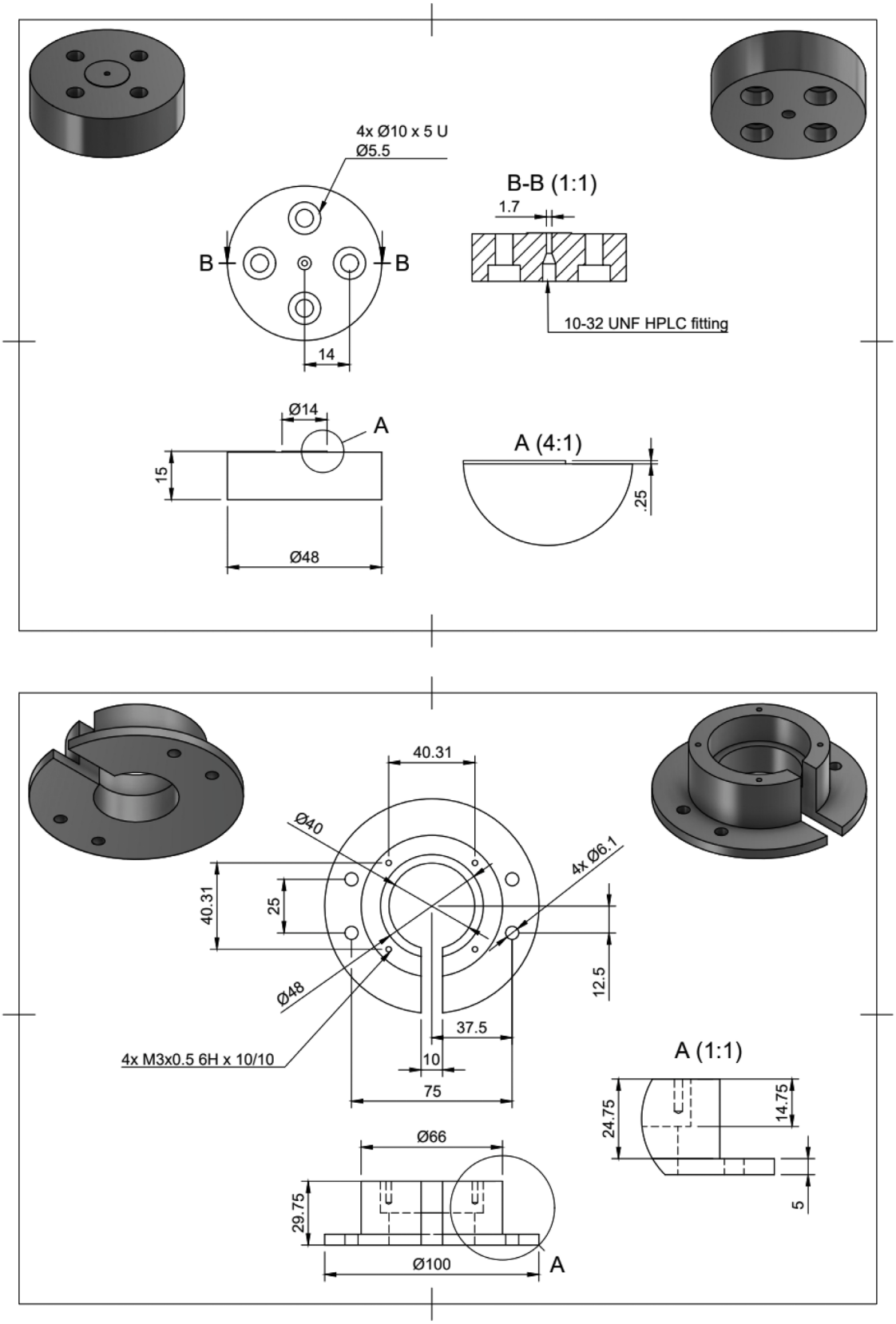

Fig. A.6. (*continued*).

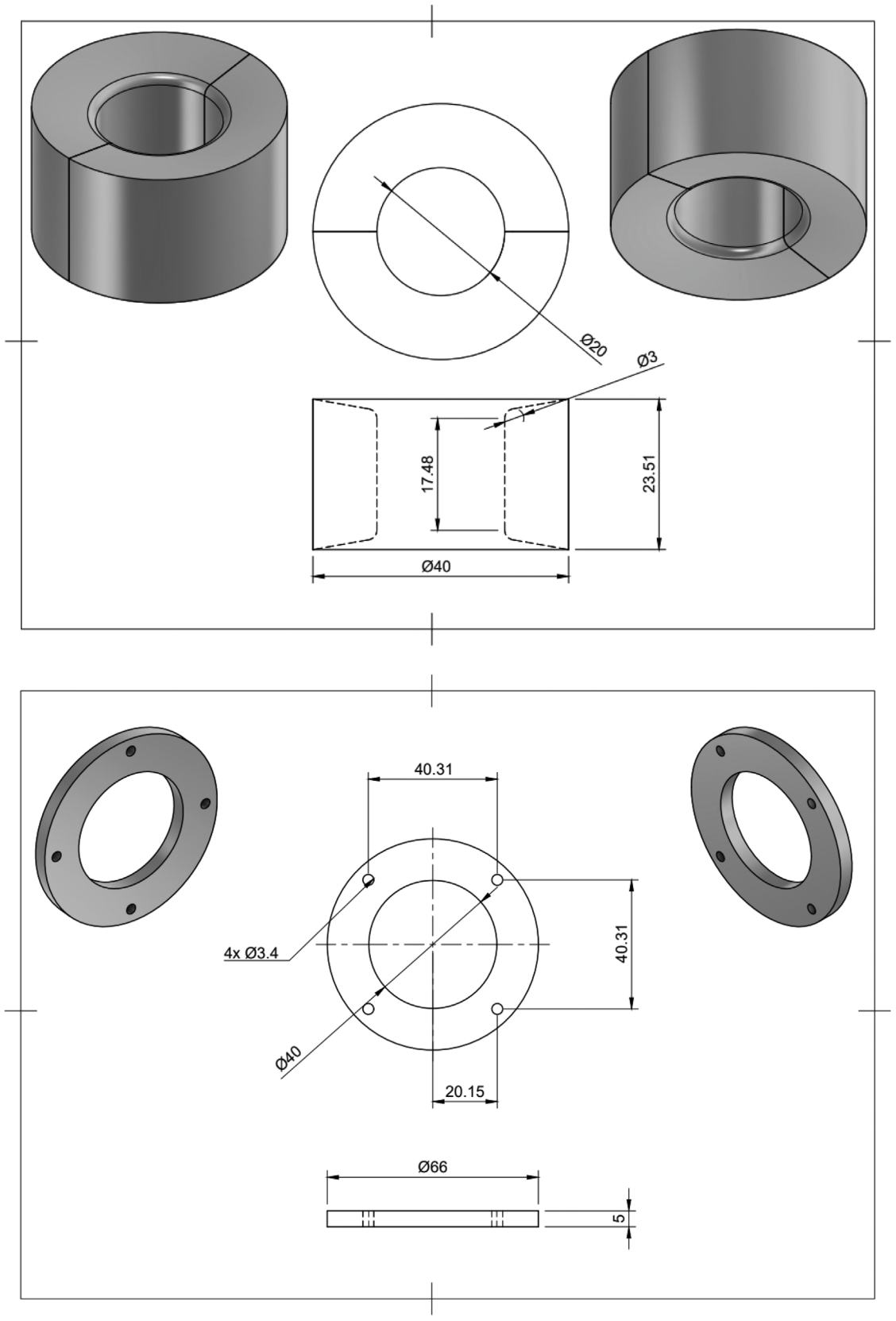

Fig. A.6. (*continued*).

References

Adeoye, J.T., et al., 2017. Effect of transport limitations and fluid properties on reaction products in fractures of unaltered and serpentinized basalt exposed to high PCO2 fluids. Int. J. Greenhouse Gas Control (ISSN: 1750-5836) 63, 310–320, URL https://www.sciencedirect.com/science/article/pii/S1750583617300592.

Ayob, A., Tamin, N., Elbasheer, M., 2009. Pressure limits of thick-walled cylinders. Lecture Notes Eng. Comput. Sci. 2.

Benson, S., et al., 2018. Underground geological storage. p. 82, IPCC Special Report 2018.

Callow, B., Falcon-Suarez, I., Ahmed, S., Matter, J., 2018. Assessing the carbon sequestration potential of basalt using X-ray micro-CT and rock mechanics. Int. J. Greenhouse Gas Control (ISSN: 1750-5836) 70, 146–156, URL http://www.sciencedirect.com/science/article/pii/S1750583617306345.

Clark, D.E., et al., 2020. CarbFix2: CO2 and H2S mineralization during 3.5 years of continuous injection into basaltic rocks at more than 250 C. Geochim. Cosmochim. Acta 279, 45–66, URL http://www.sciencedirect.com/science/article/pii/S0016703720302106.

Committee on Climate Change, 2019. Net-Zero: The UKs contribution to stopping global warming. Tech. rep, Committee on Climate Change, URL https://www.theccc.org.uk/wp-content/uploads/2019/05/Net-Zero-The-UKs-contribution-to-stopping-global-warming.pdf.

Czerwinski, F., 2020. Thermal Stability of Aluminum Alloys. Materials (ISSN: 1996-1944) 13 (15), 3441, URL https://www.mdpi.com/1996-1944/13/15/3441.

Farrell, K., 1995. Assessment of aluminum structural materials for service within the ANS reflector vessel. Tech. rep ORNL/TM–13049, 201578, Oak Ridge National Laboratory, URL http://www.osti.gov/servlets/purl/201578-2NXTy6/webviewable/.

Gadikota, G., Matter, J., Kelemen, P., Brady, P.V., Park, A.-H.A., 2020. Elucidating the differences in the carbon mineralization behaviors of calcium and magnesium bearing alumino-silicates and magnesium silicates for CO2 storage. Fuel (ISSN: 0016-2361) 277, 117900, URL http://www.sciencedirect.com/science/article/pii/S0016236120308966.

Galeczka, I., Wolff-Boenisch, D., Oelkers, E.H., Gislason, S.R., 2014. An experimental study of basaltic glass–H2O–CO2 interaction at 22 and 50°C: Implications for subsurface storage of CO2. Geochim. Cosmochim. Acta (ISSN: 0016-7037) 126, 123–145, URL https://www.sciencedirect.com/science/article/pii/S0016703713006169.

Gislason, S.R., Oelkers, E.H., 2003. Mechanism, rates, and consequences of basaltic glass dissolution: II. An experimental study of the dissolution rates of basaltic glass as a function of pH and temperature. Geochim. Cosmochim. Acta (ISSN: 00167037) 67 (20), 3817–3832, URL https://linkinghub.elsevier.com/retrieve/pii/S0016703703001765.

Gunnarsson, I., et al., 2018. The rapid and cost-effective capture and subsurface mineral storage of carbon and sulfur at the CarbFix2 site. Int. J. Greenhouse Gas Control (ISSN: 1750-5836) 79, 117–126, URL http://www.sciencedirect.com/science/article/pii/S1750583617309593.

Gysi, A.P., 2017. Numerical simulations of CO2 sequestration in basaltic rock formations: challenges for optimizing mineral-fluid reactions. Pure Appl. Chem. (ISSN: 0033-4545, 1365-3075) 89 (5), 581–596, URL https://www.degruyter.com/view/journals/pac/89/5/article-p581.xml.

Hanna, R.D., Ketcham, R.A., 2017. X-ray computed tomography of planetary materials: A primer and review of recent studies. Geochemistry (ISSN: 0009-2819) 77 (4), 547–572, URL https://www.sciencedirect.com/science/article/pii/S0009281916301064.

Hellevang, H., Haile, B.G., Tetteh, A., 2017. Experimental study to better understand factors affecting the CO $_2$ mineral trapping potential of basalt: Original research Article: Experimental study to better understand factors affecting the CO $_2$ mineral. Greenhouse Gases Sci. Technol. (ISSN: 21523878) 7 (1), 143–157, URL http://doi.wiley.com/10.1002/ghg.1619.

IEA, 2022. Carbon Capture, Utilisation and Storage. Tech. rep, IEA, URL https://www.iea.org/reports/carbon-capture-utilisation-and-storage-2.

Kahl, W.-A., Hansen, C., Bach, W., 2016. A new X-ray transparent flow-through reaction cell for a micro-CT-based concomitant surveillance of the reaction progress of hydrothermal mineral-fluid interactions. URL https://se.copernicus.org/preprints/se-2016-25/se-2016-25.pdf.

Kanakiya, S., Adam, L., Esteban, L., Rowe, M.C., Shane, P., 2017. Dissolution and secondary mineral precipitation in basalts due to reactions with carbonic acid. J. Geophys. Res. Solid Earth (ISSN: 2169-9356) 122 (6), 4312–4327, URL https://agupubs.onlinelibrary.wiley.com/doi/abs/10.1002/2017JB014019.

Kumar, A., Shrivastava, J.P., Pathak, V., 2017. Mineral carbonation reactions under water-saturated, hydrothermal-like conditions and numerical simulations of CO2 sequestration in tholeiitic basalt of the Eastern Deccan Volcanic Province, India. Appl. Geochem. (ISSN: 0883-2927) 84, 87–104, URL http://www.sciencedirect.com/science/article/pii/S0883292717302196.

Larsen, L.M., Waagstein, R., Pedersen, A.K., Storey, M., 1999. Trans-Atlantic correlation of the Palaeogene volcanic successions in the Faeroe Islands and East Greenland. J. Geol. Soc. 156 (6), 1081–1095, ISSN: 0016-7649, 2041-479X, URL https://www.lyellcollection.org/doi/10.1144/gsjgs.156.6.1081.

Luhmann, A.J., et al., 2017a. Permeability, porosity, and mineral surface area changes in basalt cores induced by reactive transport of CO2-rich brine. Water Resour. Res. (ISSN: 1944-7973) 53 (3), 1908–1927, URL https://agupubs.onlinelibrary.wiley.com/doi/abs/10.1002/2016WR019216.

Luhmann, A.J., et al., 2017b. Whole rock basalt alteration from CO2-rich brine during flow-through experiments at 150°C and 150bar. Chem. Geol. (ISSN: 0009-2541) 453, 92–110, URL https://www.sciencedirect.com/science/article/pii/S0009254117300669.

Marieni, C., Přikryl, J., Aradóttir, E.S., Gunnarsson, I., Stefánsson, A., 2018. Towards 'green' geothermal energy: Co-mineralization of carbon and sulfur in geothermal reservoirs. Int. J. Greenhouse Gas Control (ISSN: 1750-5836) 77, 96–105, URL http://www.sciencedirect.com/science/article/pii/S1750583618300252.

Menefee, A.H., Ellis, B.R., 2021. Carbon mineralization in reactive silicate zones. ACS ES&T Eng. 1 (8), 1193–1204. http://dx.doi.org/10.1021/acsestengg.1c00066, Publisher: American Chemical Society.

Menefee, A., Giammar, D., Ellis, B., 2019. Controls on Mineral Carbonation Reactions in Basalt Fracture Networks. SSRN Scholarly Paper ID 3366090, Social Science Research Network, Rochester, NY, URL https://papers.ssrn.com/abstract=3366090.

Nelson, C., Goldberg, D., White, M., Slagle, A., 2022. Optimizing Injection Strategies for Co2 Storage and Mineralization in Basalt Through Multiphase Subsurface Reservoir Simulations. SSRN Scholarly Paper, Rochester, NY, URL https://papers.ssrn.com/abstract=4280798.

Ratouis, T.M.P., et al., 2022. Carbfix 2: A transport model of long-term CO2 and H2S injection into basaltic rocks at Hellisheidi, SW-Iceland. Int. J. Greenhouse Gas Control (ISSN: 1750-5836) 114, 103586, URL https://www.sciencedirect.com/science/article/pii/S1750583622000081.

Raza, A., Glatz, G., Gholami, R., Mahmoud, M., Alafnan, S., 2022. Carbon mineralization and geological storage of CO2 in basalt: Mechanisms and technical challenges. Earth-Sci. Rev. (ISSN: 0012-8252) 229, 104036, URL https://www.sciencedirect.com/science/article/pii/S0012825222001209.

Shukla, P., Skea, J., Slade, R., Al Khourdajie, A., van Diemen, R., McCollum, D., Pathak, M., Some, S., Vyas, P., Fradera, R., Belkacemi, M., Hasija, A., Lisboa, G., Luz, S., Malley, J. (Eds.), 2022. Summary for policymakers. In: Climate Change 2022: Mitigation of Climate Change. Contribution of Working Group III to the Sixth Assessment Report of the Intergovernmental Panel on Climate Change. Cambridge University Press, URL https://www.ipcc.ch/report/ar6/wg3/downloads/report/IPCC_AR6_WGIII_SummaryForPolicymakers.pdf.

Sissmann, O., et al., 2014. Enhanced olivine carbonation within a basalt as compared to single-phase experiments: Reevaluating the potential of CO $_2$ mineral sequestration. Environ. Sci. Technol. 48 (10), 5512–5519, ISSN: 0013-936X, 1520-5851, URL https://pubs.acs.org/doi/10.1021/es405508a.

Snæbjörnsdóttir, S.Ó., et al., 2020. Carbon dioxide storage through mineral carbonation. Nat. Rev. Earth Environ. (ISSN: 2662-138X) 1 (2), 90–102, Number: 2 Publisher: Nature Publishing Group, URL https://www.nature.com/articles/s43017-019-0011-8.

UNFCCC, 0000, Nationally Determined Contributions Registry | UNFCCC, URL https://unfccc.int/NDCREG.

Vlassenbroeck, J., et al., 2006. Octopus 8: a high performance tomographic reconstruction package for X-ray tube and synchrotron micro-CT. In: Advances in X-Ray Tomography for Geomaterials. John Wiley & Sons, Ltd, ISBN: 978-0-470-61218-7, pp. 167–173, URL https://onlinelibrary.wiley.com/doi/abs/10.1002/9780470612187.ch13.

Voigt, M., et al., 2021. An experimental study of basalt–seawater–CO2 interaction at 130 °C. Geochim. Cosmochim. Acta (ISSN: 0016-7037) 308, 21–41, URL https://www.sciencedirect.com/science/article/pii/S0016703721003379.

Wang, F., Dreisinger, D., Jarvis, M., Hitchins, T., 2019. Kinetics and mechanism of mineral carbonation of olivine for CO2 sequestration. Minerals Eng. (ISSN: 0892-6875) 131, 185–197, URL http://www.sciencedirect.com/science/article/pii/S0892687518305077.

Xing, T., Zhu, W., Fusseis, F., Lisabeth, H., 2018. Generating porosity during olivine carbonation via dissolution channels and expansion cracks. Solid Earth (ISSN: 1869-9529) 9 (4), 879–896, URL https://www.solid-earth.net/9/879/2018/.

Xiong, W., et al., 2017. CO2 mineral trapping in fractured basalt. Int. J. Greenhouse Gas Control (ISSN: 1750-5836) 66, 204–217, URL http://www.sciencedirect.com/science/article/pii/S1750583617305595.

Xiong, W., et al., 2018. CO $_2$ Mineral Sequestration in Naturally Porous Basalt. Environ. Sci. Technol. Lett. (ISSN: 2328-8930, 2328-8930) 5 (3), 142–147, URL https://pubs.acs.org/doi/10.1021/acs.estlett.8b00047.

Zhu, W., et al., 2016. Experimental evidence of reaction-induced fracturing during olivine carbonation: Fracturing during olivine carbonation. Geophys. Res. Lett. (ISSN: 00948276) 43 (18), 9535–9543, URL http://doi.wiley.com/10.1002/2016GL070834.